

# International Conference on Space Optics—ICSO 2022

Dubrovnik, Croatia

3–7 October 2022

*Edited by Kyriaki Minoglou, Nikos Karafolas, and Bruno Cugny,*



## *SPEXone multi-angle spectropolarimeter characterization, calibration, and key data derivation using the L0-1B processor*



# SPEXone multi-angle spectropolarimeter characterization, calibration, and key data derivation using the L0-1B processor

Jeroen Rietjens<sup>a</sup>, Martijn Smit<sup>a</sup>, Jochen Campo<sup>a</sup>, Thomas Bouchan<sup>a,b</sup>, Ryan Cooney<sup>a</sup>, Pierre Piron<sup>a,c</sup>, Paul Tol<sup>a</sup>, Raul Laasner<sup>a</sup>, Richard van Hees<sup>a</sup>, Jochen Landgraf<sup>a</sup>, and Otto Hasekamp<sup>a</sup>

<sup>a</sup>SRON Netherlands Institute for Space Research, Niels Bohrweg 4, 2333 CA Leiden, the Netherlands

<sup>b</sup>TNO, Optics Department, Stieltjesweg 1, 2628 CK Delft, The Netherlands

<sup>c</sup>Delft University of Technology, Kluyverweg 1, 2629 HS Delft, the Netherlands

## ABSTRACT

In the past few years, the SPEXone instrument has been developed, tested, calibrated and delivered to the NASA PACE (Plankton Aerosol and Ocean Ecosystems) project by a Dutch consortium consisting of SRON and Airbus Defence and Space Netherlands with support from TNO. Onboard the PACE satellite, SPEXone will fly together with the Ocean Color Instrument (OCI) and the Hyper-Angular Rainbow Polarimeter 2 (HARP2).

SPEXone is a compact multi-angle channeled spectropolarimeter with five viewing angles and hyperspectral imaging of a  $\sim 100$  km swath with a spatial resolution of  $4.6 \times 5.4$  km in the along-track and across-track directions and a spatial oversampling ratio of 2. SPEXone has a spectral range from 385 to 770 nm and a spectral resolution slightly below 2 nm. High accuracy polarimetry is achieved by implementation of the dual-beam snapshot spectral polarization modulation concept, yielding two complementary spectrally modulated hyperspectral images of the same scene from which both radiance and state of linear polarization can be extracted.

This paper presents results from the characterization and on-ground calibration campaign of SPEXone and discusses the use of the L0-L1B processor to derive the calibration key data (CKD) that is required for the operational data processing. The L0-L1B data processor has been developed in such a way that the CKD derivation is fully consistent with the L0-L1B processing steps, meaning that the data from which the CKD at a certain processing step is derived has been processed using the CKD from all previous processing steps. The processing steps that have been implemented include those related to the detector characterization (dark offset and dark current, non-linearity, and pixel-response non-uniformity), and those related to the instrument calibration (stray light, field-of-view, line-of-sight, wavelength, radiometric and polarimetric).

We will show examples of the derived CKD and their use in the processing of measurement data. We will demonstrate the performance of the polarimetric calibration by comparing SPEXone measurement results against a well characterized polarization state generator, showing differences of the order of a few times 0.001 in the degree of linear polarization. In addition, we will discuss the approach for the implementation of a stray light correction algorithm that has the potential to correct diffuse stray light with a spectral intensity and possibly size variation of the kernel, and that can correct moving ghosts with a constant kernel shape.

**Keywords:** spectropolarimetry, spectral modulation, multi-angle, remote sensing, atmospheric aerosol, SPEXone, PACE

## 1. INTRODUCTION

In the past few years, the SPEXone multi-angle spectropolarimeter<sup>1</sup> has been developed, tested, calibrated and delivered to the NASA PACE (Plankton Aerosol and Ocean Ecosystems) project<sup>2</sup> by a Dutch consortium consisting of SRON and Airbus Defence and Space Netherlands with support from TNO. Onboard the PACE satellite, which is developed by NASA Goddard Space Flight Center (GSFC) and which has a targeted launch

---

Corresponding author: Jeroen Rietjens, e-mail: j.h.h.rietjens@sron.nl

date in January 2024, SPEXone will fly together with the Ocean Color Instrument (OCI) and the Hyper-Angular Rainbow Polarimeter 2 (HARP2).<sup>3</sup> The PACE mission has a minimum duration of three years, with orbit maintenance capabilities for 10 years. The PACE mission will make global observations of the atmosphere and ocean surface, with the goal to understand and quantify the global biogeochemical cycling and ecosystem function in response to anthropogenic and natural environmental variability and change. SPEXone aims to deliver high quality hyperspectral multi-angle radiance and polarization products that, together with products from OCI and HARP2, enable unprecedented aerosol and cloud characterization from space.

The integrated SPEXone instrument has been characterized and calibrated on-ground in the period between November 2020 and May 2021, while the detector was characterized prior to integration about one year earlier. The first full instrument calibration took place at SRON in the Netherlands, while a second, so-called cross-calibration, took place at NASA GSFC. The latter had a limited scope and focused on the radiometric and polarimetric calibration of the instrument, serving as an independent second calibration and allowing for direct comparison of calibration results with those from the HARP2 instrument, which will be calibrated in the same lab. The focus of this paper are the on-ground calibration activities taken at SRON.

In parallel with the development of the instrument, the L0-L1B data processor has been developed that will be used for the operational data processor, but is also used for the derivation of the calibration key data (CKD). Therefore, the L0-L1B data processor has been developed in such a way that the CKD derivation is fully consistent with L0-L1B processing steps, meaning that the data from which the CKD at a certain processing step is derived has been processed using the CKD from all previous processing steps.

This paper will give a brief overview of the calibration campaign and present the approach taken for the L0-L1B data processor. The calibration measurements are closely related to L0-L1B processing steps and an example of such measurements and the algorithm used for processing this measurement is presented. This paper is organised as follows. Section 2 gives a short overview of the main characteristics of the SPEXone instrument. A concise overview of the on-ground calibration campaign is presented in Section 3. Section 4 discusses the L0-L1B processing in more detail, with the focus on several key processing algorithms. Section 5 presents a set of key calibration measurements and the CKD that is derived from those measurements, as well as an example of a polarimetric verification measurement obtained with a polarization state generator. Stray light is addressed in Section 6 and focuses on an algorithm capable of correcting stray light with a wavelength dependent intensity. Finally, Section 7 summarizes the main conclusion and gives an outlook to future activities in preparation for the in-orbit operation of the SPEXone instrument.

## 2. SPEXONE INSTRUMENT

SPEXone is a compact multi-angle channeled spectropolarimeter that fits within an envelope of 150 mm x 290 mm x 370 mm. It uses spectral polarization modulation<sup>4</sup> to accurately measure the state of linear polarization of the incident light in the spectral range from 385 to 770 nm. Spectral polarization modulation is a polarimetry technique that enables snapshot spectropolarimetry with high accuracy without moving parts using a combination of fixed retarders and polarizers. In SPEXone, a dual beam version is implemented that provides two complementary spectral images per viewing angle and not only leads to a low sensitivity to systematic effects, but also allows the reconstruction of the absolute radiance spectrum at the spectral resolution of the spectrometer.

SPEXone has five viewing angles at  $-50^\circ$ ,  $-20^\circ$ ,  $0^\circ$ ,  $+20^\circ$ , and  $+50^\circ$  at instrument level. Each viewing angle offers hyperspectral imaging capability of a swath slightly larger than 100 km, leading, with yaw compensation at satellite level, to a common swath of about 100 km. Each swath is imaged twice, yielding 10 spectral images at the focal plane with a spatial resolution of 4.6 x 5.4 km in the along-track and across-track directions and with a spatial oversampling ratio of 2. SPEXone has a spectral range from 385 to 770 nm and a spectral resolution slightly below 2 nm.

At the spectrometer focal plane, SPEXone uses a compact camera module from 3Dplus that is equipped with a CMOSIS CMV4000 CMOS image sensor, a Field-Programmable Gate-Array (FPGA), SDRAM and flash memory.<sup>5</sup> Raw 2k x 2k images are acquired by the CMOS detector at a rate of 15 Hz. 5 subsequent images are co-added and binned in order to reduce the data volume of a single final image to  $\approx 200$  kpixel. Image

acquisition, binning and co-adding operations are all executed within the DEM by the FPGA using dedicated firmware.

The camera module is embedded in the detector module (DEM) that is controlled at a constant temperature within  $\pm 0.15$  K. A radiator provides sufficient cooling power to the DEM and also serves as a heat sink for the opto-mechanics, which allows controlling the temperature of the optics within  $\pm 1$  K while operating at room temperature.<sup>6</sup> Two (redundant) LEDs can provide a smooth illumination of the focal plane for detector monitoring at the native pixel level during the eclipse.

The Instrument Control Unit (ICU) is a separate unit that powers and commands the DEM, controls the internal calibration LEDs, performs thermal control of the DEM and instrument opto-mechanics, handles the science and housekeeping data acquisition and communicates with the satellite.

### 3. ON-GROUND CALIBRATION CAMPAIGN

The on-ground calibration of both the detector and the integrated SPEXone instrument have been performed in an optical cleanroom under ambient conditions. This approach has been chosen largely in view of design-to-cost project constraints, but was justified based on analysis of optical differences between an ambient and vacuum environment, the use of dense optical coatings, and the execution of vacuum calibration spot checks. The latter were taken as part of the thermal balance in vacuum test and had a focus on the polarimetric response of the system. The on-ground calibration consisted of several measurement sequences from which corresponding CKD has been derived, and that are listed in Table 1.

The detector calibration setup and procedure has been described in.<sup>5</sup> The instrument calibration setup will be described in detail a future paper, but is summarized here. The SPEXone instrument was mounted on a mechanical structure consisting of two orthogonal rotation stages allowing for accurate instrument alignment in the across-track (ACT) and along-track (ALT) directions. The latter includes the full viewing angle range of  $\pm 50^\circ$ . In order to be able to thermally control the instrument to the operational in-flight temperature, a cooling plate was mounted to the radiator, providing sufficient cooling for the detector and instrument. Condensation onto the instrument and radiator was prevented by placing the full setup in a black enclosure that could be purged with dry nitrogen. Since also the light sources had to be placed inside the enclosure, particular attention was paid to provide sufficient baffling in order to minimize background light.

Two main light sources have been employed during the calibration campaign, a collimator and an integrating sphere. The collimator was in-house developed and based on a high performance off-axis parabolic mirror. The collimator provided a uniform, narrow-angle light beam of sufficient diameter to cover the full swath of all viewing angles using only the rotation stages. The collimator was used with a pinhole, providing a narrow field in two dimensions required for the spatial assignment measurements, as well as with a narrow slit, providing full illumination of spectrometer slit in the ALT direction only and was used during field-of-view and stray light calibration. The alignment between the collimator and the instrument was regularly checked using a theodolite and reference surfaces on both the collimator and the instrument. The integrating sphere was a radiometrically calibrated version from Labsphere with a 4 inch exit port, providing both spatial and angular uniform illumination covering the full swath for all viewing angles. During polarimetric calibration a rotating ultra-broadband wire-grid polarizer was inserted between integrating sphere and instrument, while during the polarimetric verification measurements the rotating polarizer was replaced by a set of counter-rotating tilting glass plates.

Table 1: Calibration measurement sequences from which corresponding CKD is derived.

Processing on detector (full frame) level	Processing on extracted spectra level
1. Detector offset	7. Instrument field-of-view
2. Detector dark current	8. Instrument line-of-sight
3. Detector noise	9. Instrument wavelength calibration
4. Detector non-linearity	10. Instrument radiometric calibration
5. Detector pixel-response non-uniformity	11. Instrument polarimetric calibration
6. Instrument stray light	12. Instrument polarimetric verification

Table 2: Data processing levels for LEO data.

Data level	Description
0	Instrument and auxiliary data reconstructed from satellite raw data after removing communication artifacts
1	Instrument data extracted at full original resolution, with geolocation and calibration information
1A	Instrument counts with geolocation and calibration information attached but not applied
1B	Geolocation and calibration information applied to the instrument counts
1C	Level 1B data collocated to a common grid for all viewing angles
2	Geophysical quantity retrieved from single instrument data from level 1C data

Both collimator and integrating sphere could be connected to fiber based light sources. We used a set of seven diode lasers (405 nm, 457 nm, 515 nm, 561 nm, 660 nm, 732 nm, and 785 nm) from Cobolt/Hübner and Crystalaser, and a laser-driven white-light source from Energetiq. In addition, the integrating sphere was equipped with a radiometrically calibrated internal halogen lamp.

#### 4. L0-L1B PROCESSOR

The SPEXone data philosophy follows the WMO and NASA data processing levels for LEO data, which is summarized up to level 2 in Table 2.

The conversion from L0 to L1A is an independent processing step and involves mainly rearranging the contents of science and housekeeping CCSDS packets into the L1A NetCDF format. The L1A-L1B processor is set up to sequentially process the L1A flight data into L1B data in  $N$  calibration steps  $P_1$  to  $P_N$ . After each step, the calibration level of the data increases from  $L1A_0$  to  $L1A_N$ , starting with  $L1A_0$  which is the original L1A data, up to  $L1A_N$  which is the final L1B product, see Fig. 1a. Processing of the CKD for level  $n$  from the on-ground calibration measurements  $cL1A^n$  is illustrated in Fig. 1b.

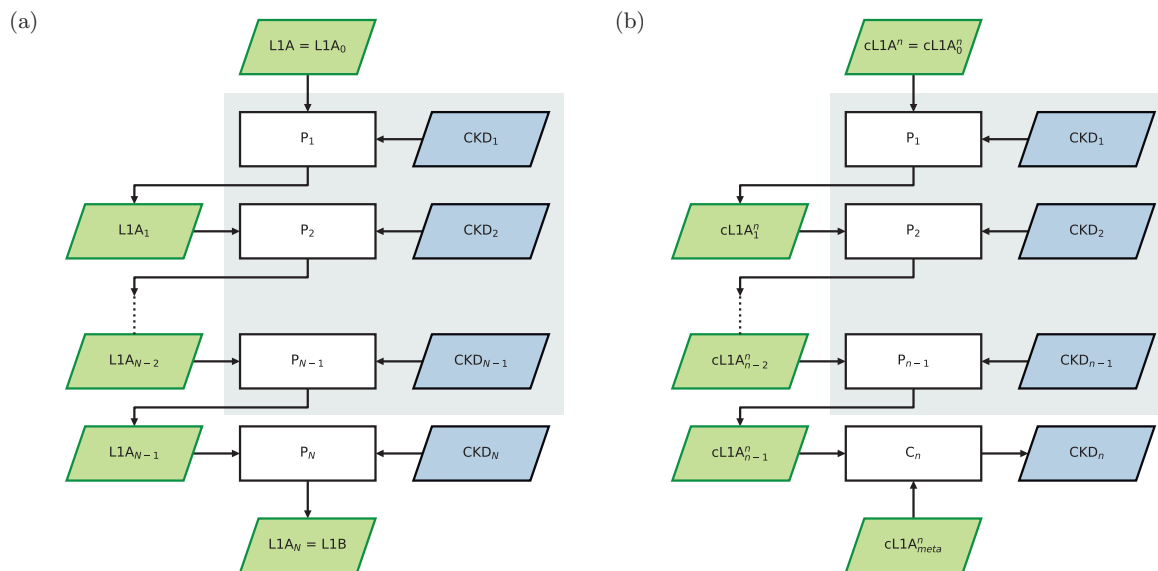


Figure 1: a) Illustration of the stepwise L1A-L1B processor. The grey area shows processor elements that are also used by the CKD processor. b) Illustration of the stepwise CKD processor and its interdependence with the L1A-L1B processor.  $cL1A_l^n$  refers to a calibration measurement calibrated up to level  $l$  and used for deriving the CKD of step  $n$ . The grey area shows processor elements that are common with the L1A-L1B processor.

First, the measurements are calibrated up to level  $n - 1$ , cL1A $_{n-1}^n$ , using the processing steps  $P_1$  to  $P_{n-1}$  of the L1A-L1B processor and the corresponding key data CKD $_1$  to CKD $_{n-1}$ . For step  $n$ , the key data CKD $_n$  are generated by a dedicated processing step  $C_n$  of the CKD processor. This procedure has to be followed for the CKD measurements of level 1 to  $N$  and so it sequentially generates the key data set (CKD $_1, \dots, \text{CKD}_N$ ). An important aspect of the sketched processor architecture is that the key data of level  $n$  depends on the corresponding data of lower hierarchy CKD $_1$  to CKD $_{n-1}$ . This means that for any update of the key data of a certain level, reprocessing of higher level data is required. The interdependence of both processors is seen when comparing both figures. Here the flight data processing depends on the derived key data and the CKD processor uses the L1A-L1B processing steps  $P_1$  to  $P_{n-1}$  to calibrate the on-ground calibration measurements. Therefore, both processors have to be harmonized and are provided as one software package, though only the L1A-L1B processor needs to be run continuously during operation.

## 5. CKD DERIVATION

As an illustration of the steps listed in Table 1, we show examples of calibration measurements and the derived CKD from those measurements in Fig. 2. We start here with a field-of-view calibration measurement, so we assume all detector characterization measurements<sup>5</sup> have already been processed into the corresponding CKD. These CKD, corresponding to processing steps 1-5 in Table 1, are applied to all measurement data. Stray light correction is not yet applied here. As mentioned in Section 3, a field-of-view measurement is taken with the collimator, so only a single spatial resolution element is illuminated, yielding a narrow spectrum on the detector that is curved due to keystone in the optical image. The processor fits the vertical position of this spectrum in each column as CKD, which allows to extract a spectrum from a single ground pixel when the full swath is illuminated. Fig. 2b shows these positions for a subset of spatial resolution elements within the swath of viewing angle  $-20^\circ$ .

Similarly, the horizontal positions of the slit images of the wavelength calibration measurements are fitted for each spectrum using the field-of-view CKD. Subsequently, these positions are interpolated using a polynomial in order to obtain the wavelengths associated with each element of the spectrum. Fig. 2d shows the full wavelength CKD of the instrument projected on the detector area.

The radiometric calibration is performed on spectra extracted from measurements during which the instrument is illuminated with an unpolarized and radiometrically calibrated light source, using the field-of-view and wavelength CKD. The radiometric CKD is plotted in Fig. 2f as a projection on the detector area.

Finally, polarimetric calibration is performed starting with radiometrically calibrated spectra extracted from measurements during which the instrument is illuminated with fully polarized light, using all CKD derived in previous steps. In order to derive the polarimetric CKD, which corresponds to the Mueller matrix element  $M_q$  and  $M_u$  (or, when combined, the polarimetric efficiency), data from 24 measurements with different orientations ( $0^\circ$ - $360^\circ$  in steps of  $15^\circ$ ) of the polarizer are used. The 24 modulated spectra are fitted with a model with the spectral retardance of the PMO and the Mueller matrix element  $M_q$  and  $M_u$  as fitting parameters. The polarimetric CKD is plotted as the polarimetric efficiency of each viewing angle in Fig. 2h.

For verification of the polarimetric calibration, measurements were taken using a polarization state generator (PSG) based on a set of tilting fused silica glass plates. The PSG was independently characterized using a rotating ultra-broadband wire grid polarizer. The PSG provides light with a degree of linear polarization between 0 and  $\approx 0.35$  at an arbitrary angle of polarization. The extracted DoLP obtained from measurements by SPEXone at several different glass plate angles at an AoLP of  $0^\circ$  is shown in Fig. 3a for data obtained with viewing angle  $+50^\circ$  illuminated. The comparison of these DoLPs with the PSG characterization data is shown in Fig. 3b. It can be seen that the RMS difference per glass plate angle is smaller than 0.001 for DoLP up to 0.1, and that this RMS difference increases to 0.0025 at higher DoLPs. Also, a clear variation of the difference versus wavelength can be observed for the larger DoLPs at larger glass plate angles. The largest negative difference (up to -0.0035) occurs in the blue, the largest positive difference (up to +0.005) in the green, and the best agreement in the red part of the spectrum. This systematic difference is subject of further investigation, as it could be related to both the PSG characterization and the SPEXone calibration.

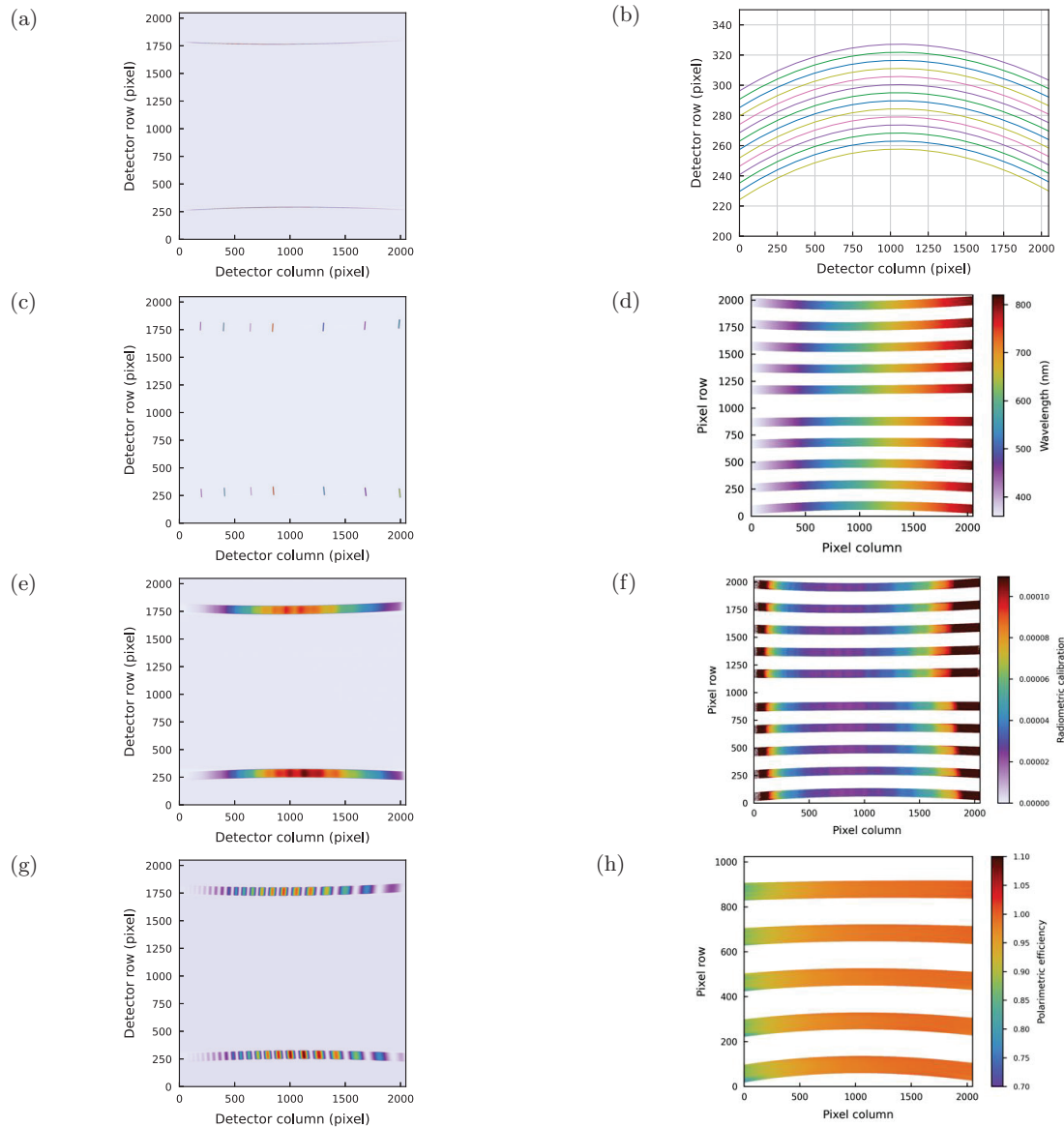


Figure 2: Examples of single measurements with viewing angle  $-20^\circ$  illuminated and derived CKD. a) Field-of-view measurement showing two narrow white light spectra. b) Derived spectral detector positions of a subset of spatial sampling elements. c) Wavelength calibration measurement showing 7 monochromatic (full) slit images corresponding to the 7 diode lasers. d) Wavelength map using data from all viewing angles. e) Radiometric calibration measurement using the unpolarized calibrated output of the integrating sphere. f) Derived radiometric CKD using data from all viewing angles. g) Polarimetric calibration measurement using fully polarized light. h) Derived polarimetric efficiency using data from all viewing angles.

## 6. STRAY LIGHT

Stray light is the dominant contributor to the absolute radiometric and systematic polarimetric errors in non-uniform scenes, see.<sup>7</sup> Based on early stray light analysis results from ZEMAX, an algorithm was developed that focused on correcting for diffuse stray light and for a moving ghost. Initially, the shape and intensity (i.e. the kernel) of both the diffuse stray light and ghost were assumed constant. The diffuse ( $\mathbf{K}^{\text{diffuse}}$ ) and ghost ( $\mathbf{K}^{\text{ghost}}$ )

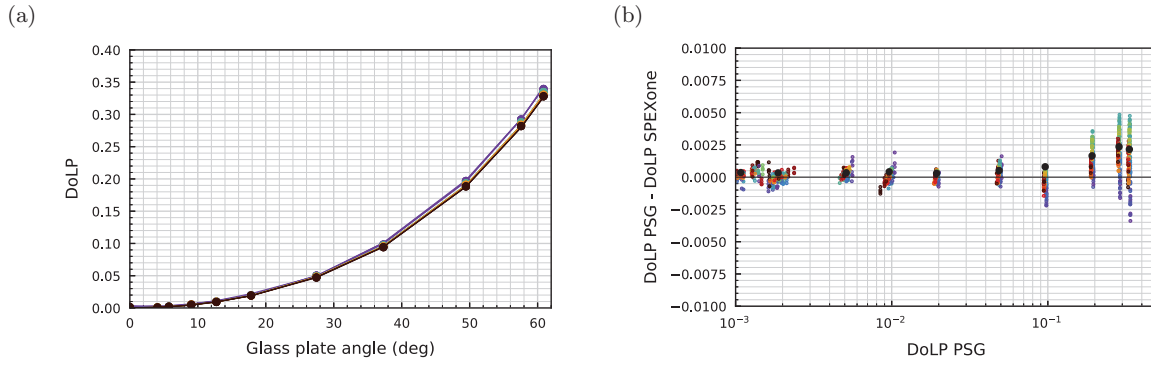


Figure 3: Verification of the polarimetric calibration of SPEXone by comparing processed PSG measurements taken with viewing angle  $+50^\circ$  illuminated with the PSG characterization data. Colors are indicative of the wavelength at which the DoLP is compared, while the black dots show the RMS difference per glass plate angle.

stray light kernels, including the parameters describing the movement of the ghost with respect to the diffuse kernel would be extracted by fitting stray light calibration measurements. The stray light CKD, consisting of the kernels and movement parameters, are then applied to measurement images using a Van Cittert deconvolution algorithm based on fast Fourier transforms.<sup>8,9</sup> The goal is to obtain the clean signal  $\mathbf{S}^{\text{ideal}}$  from the recorded signal  $\mathbf{S}^{\text{rec}}$  that has been convolved with the stray light kernels  $\mathbf{K}^{\text{diffuse}}$  and  $\mathbf{K}^{\text{ghost}}$ . These quantities are related by

$$\mathbf{S}_{ij}^{\text{rec}} = (1 - \eta)\mathbf{S}_{ij}^{\text{ideal}} + \sum_{mn} \mathbf{K}_{i-m, j-n}^{\text{diffuse}} \mathbf{S}_{mn}^{\text{ideal}} + \sum_{mn} \mathbf{K}_{i-m+f_r(m), j-n+f_c(n)}^{\text{ghost}} \mathbf{S}_{mn}^{\text{ideal}} \quad (1)$$

in which  $i$  and  $j$  represent indices of a certain detector pixel,  $m$  and  $n$  the pixel indices used in the summation as part of the convolution, and  $f_{r,c}$  the function that describes the ghost movement in the row and column direction. The last term in Eq. (1) cannot be directly computed using fast Fourier transforms because of the move functions  $f_{r,c}$  in the kernel indices. We perform a substitution of variables in which the moving indices of the ghost kernel are transferred to the original image, which is effectively a transformation of the original image,  $\mathbf{S}_{\text{ideal, tr}}$ . So instead of explicitly convolving the original image with a moving kernel, we take the ghost kernel ( $\mathbf{K}^{\text{ghost}}$ ) to be stationary (because the moving indices have been eliminated) and use a transformed version of the original image ( $\mathbf{S}^{\text{ideal}}$ ) for the convolution. The transformed image  $\mathbf{I}^{\text{ideal, tr}}$  looks similar to the original array  $\mathbf{I}^{\text{ideal}}$  but is stretched or skewed, depending on the moving ghost parameters. The Van Cittert deconvolution has, in the presence of one diffuse and one ghost kernel, the form

$$\mathbf{S}_v^{\text{ideal}} = \frac{\mathbf{S}^{\text{rec}} - (\mathbf{K}^{\text{diffuse}} \otimes \mathbf{S}_{v-1}^{\text{ideal}} + \mathbf{K}^{\text{ghost}} \otimes \mathbf{S}_{v-1}^{\text{ideal, tr}})}{1 - \eta}, \quad (2)$$

$$\eta = \sum_{mn} \mathbf{K}_{mn}^{\text{diffuse}} + \sum_{mn} \mathbf{K}_{mn}^{\text{ghost}},$$

where  $\eta$  is the internal scattering coefficient and  $v$  denotes the  $v$ th step of the algorithm which starts with  $\mathbf{S}_0^{\text{ideal}} = \mathbf{S}^{\text{rec}}$ . In practice, about four iterations are usually sufficient for convergence.

However, as discussed in,<sup>10</sup> actual stray light calibration measurements showed different characteristics of the stray light:

- The intensity of the diffuse stray light is not constant with wavelength, but decreases with increasing wavelength.
- The shape of the diffuse stray light is not constant with wavelength, but grows with increasing wavelength.
- A different moving (arc-shaped) ghost is observed that spans more pixels and is less constant in shape than the simulated moving ghost.

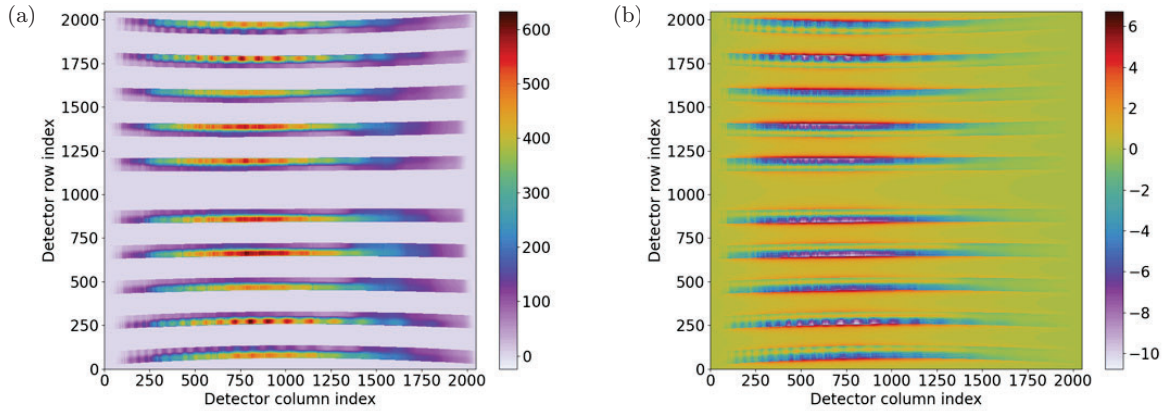


Figure 4: a) Simulated SPEXone detector image  $S_i^{\text{rec}}$  with a non-uniform high contrast scene in each of the viewing angles after convolution with a wavelength dependent diffuse kernel. b) Difference between the simulated detector image with ( $S_i^{\text{rec}}$ ) and without ( $S_i^{\text{ideal}}$ ) stray light.

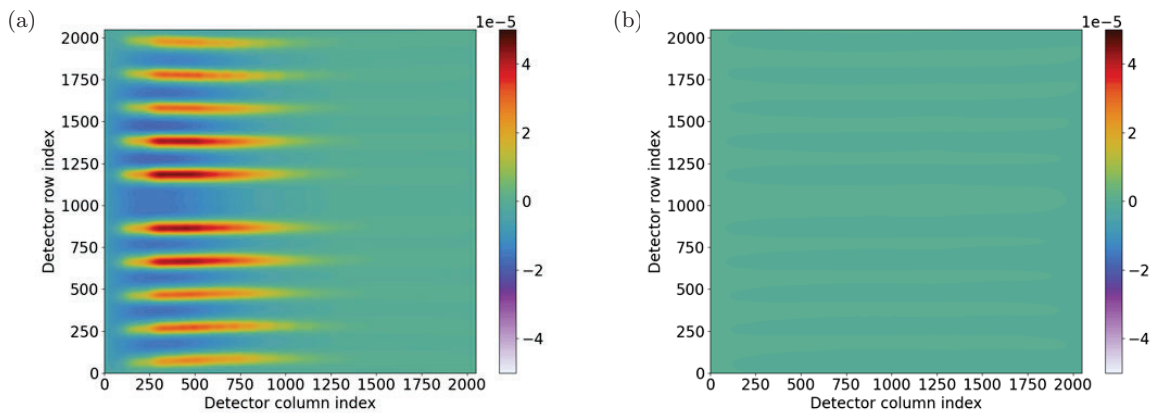


Figure 5: Difference between the simulated detector image after a) 3 ( $S_3^{\text{rec}}$ ) and b) 4 ( $S_4^{\text{rec}}$ ) Van Cittert iterations with and without stray light ( $S_i^{\text{ideal}}$ ).

In order to deal with these observed stray light features, the stray light correction algorithm needs to be updated. The intensity dependence of the diffuse stray light is taken into account by changing the internal scattering factor  $\eta$  from a constant to a pixel dependent variable in both spatial and spectral dimensions. We have developed a preliminary version of the Van Cittert algorithm that works with a pixel dependent stray light kernel. As an example, we show a simulated SPEXone scene in which for each viewing angle the swath is divided into a low and high signal part with also a DoLP contrast, see Fig. 4. For illustration  $\eta$  is chosen to have a linear wavelength dependence where it is higher at lower wavelengths but the algorithm is not restricted to such simple functional forms. The results after 3 and 4 Van Cittert iterations are plotted in Fig. 5, showing that the algorithm is capable of removing diffuse stray light with a wavelength dependent intensity.

The increasing shape of the diffuse stray light can be taken into account in the algorithm in similar manner as the moving ghost: by applying an image transformation to the original image such that a constant diffuse kernel can be used in the deconvolution process.

The effectiveness of this algorithm on the real data still needs to be assessed. The achievable correction factor will depend strongly how well the wavelength and shape dependence of the intensity can be approximated with a (simple) functional dependence, and how well the diffuse stray light kernels can be derived from the stray light calibration measurements.

## 7. CONCLUSIONS

In this paper we have presented the calibration and key data derivation approach for the SPEXone instrument. We have outlined the relation between the L0-L1B processor steps and the calibration measurement from which certain CKD is derived. We have shown examples of CKD from the full processing chain up to and including the polarimetric calibration. As an example, we compare the results from SPEXone measurements of a polarization state generator with the PSG characterization data. This comparison shows excellent agreement of the order of 0.001 or better for  $\text{DoLP} < 0.1$ , but also some systematic differences up to 0.005 for some wavelengths at  $\text{DoLP} > 0.2$ . These systematic difference are subject to further investigation. Finally, we have described the approach for the stray light correction algorithm that aims at reducing diffuse and ghost stray light to acceptable levels. As an example of the method that takes into account the wavelength dependence of the stray light intensity, we show the performance of the algorithm on simulated SPEXone measurement and demonstrate that the algorithm is capable of efficiently correcting stray light when the stray light kernels are well known. Next step is to expand the stray light correction algorithm to be able to incorporate a spatial-spectral dependence of the shape of the diffuse kernel and to test the algorithm using measured stray light kernels obtained during the on-ground calibration campaign.

## ACKNOWLEDGMENTS

SPEXone is a public-private initiative of SRON Netherlands Institute for Space Research and Airbus Defence and Space Netherlands, supported by opto-mechanical expertise from TNO. We acknowledge funding by the Ministry of Education Culture and Science (OCW), the Netherlands Space Office (NSO), and the Netherlands Organization of Scientific Research (NWO). We acknowledge NASA for hosting SPEXone on their PACE observatory as a partnered payload.

We also acknowledge our main suppliers for their contribution to realizing SPEXone; TNO, LT Ultra and NOVA ASTRON (mirror manufacturing), Optics Balzers Jena GmbH and Delta Optics (coating development), Horiba (grating), Lucassen and Kusters (precision mechanics), 3Dplus (camera module) and Hyperion Technologies (ICU).

## REFERENCES

- [1] van Amerongen, A., Rietjens, J., Campo, J., Dogan, E., Dingjan, J., Nalla, R., Caron, J., and Hasekamp, O., “SPEXone: a compact multi-angle polarimeter,” in [*International Conference on Space Optics — ICSO 2018*], Sodnik, Z., Karafolas, N., and Cugny, B., eds., **11180**, 223 – 236, International Society for Optics and Photonics, SPIE (2019).
- [2] Werdell, P. J., Behrenfeld, M. J., Bontempi, P. S., Boss, E., Cairns, B., Davis, G. T., Franz, B. A., Gliese, U. B., Gorman, E. T., Hasekamp, O., Knobelspiesse, K. D., Mannino, A., Martins, J. V., McClain, C. R., Meister, G., and Remer, L. A., “The plankton, aerosol, cloud, ocean ecosystem (pace) mission: Status, science, advances,” *Bull. Amer. Meteor. Soc.* **100**, 1775–1794 (Apr 2019).
- [3] Martins, J. V., and Chad Fish, T. N., Sparr, L., Fernandez-Borda, R., Schoeberl, M., and Remer, L., “Harp cubesat—an innovative hyperangular imaging polarimeter for earth science applications,” *Small Sat Pre-Conference Workshop, Logan Utah* (Jul 2014).
- [4] Snik, F., Karalidi, T., and Keller, C. U., “Spectral modulation for full linear polarimetry,” *Appl. Opt.* **48**, 1337–1346 (Mar 2009).
- [5] Campo, J., Tol, P., van der Vlugt, J., Smit, M., Talsma, J., Johansen, J., Eigenraam, A., van Hees, R., Hasekamp, O., Oort, M., van Amerongen, A., and Rietjens, J., “Characterization and video chain development of the CMOS detector applied in the multi-angle spectro-polarimeter SPEXone,” in [*International Conference on Space Optics — ICSO 2020*], Cugny, B., Sodnik, Z., and Karafolas, N., eds., **11852**, 459 – 470, International Society for Optics and Photonics, SPIE (2021).
- [6] van Brakel, R., van Amerongen, A., Rietjens, J., Oort, M., and Doornink, J., “Spexone polarimeter instrument thermal design,” *International Conference on Environmental Systems* (Jul 2019).

- [7] Rietjens, J., Campo, J., Chanumolu, A., Smit, M., Nalla, R., Fernandez, C., Dingjan, J., van Amerongen, A., and Hasekamp, O., “Expected performance and error analysis for SPEXone, a multi-angle channeled spectropolarimeter for the NASA PACE mission,” in [*Polarization Science and Remote Sensing IX*], Craven, J. M., Shaw, J. A., and Snik, F., eds., **11132**, 34 – 47, International Society for Optics and Photonics, SPIE (2019).
- [8] Van Cittert, P., “Zum einfluss der spaltbreite auf die intensitätsverteilung in spektrallinien. ii,” *Zeitschrift für Physik* **69**(5), 298–308 (1931).
- [9] Tol, P. J. J., van Kempen, T. A., van Hees, R. M., Krijger, M., Cadot, S., Snel, R., Persijn, S. T., Aben, I., and Hoogeveen, R. W. M., “Characterization and correction of stray light in tropomi-swir,” *Atmospheric Measurement Techniques* **11**(7), 4493–4507 (2018).
- [10] Rietjens, J. H. H., Campo, J., Smit, M., Winkelman, R., Nalla, R., Landgraf, J., Hasekamp, O., Oort, M., and van Amerongen, A., “Optical and system performance of SPEXone, a multi-angle channeled spectropolarimeter for the NASA PACE mission,” in [*International Conference on Space Optics — ICSO 2020*], Cugny, B., Sodnik, Z., and Karafolas, N., eds., **11852**, 1340 – 1350, International Society for Optics and Photonics, SPIE (2021).